

The enhanced pyrocatalysis of the pyroelectric BiFeO₃/g-C₃N₄ heterostructure for dye decomposition driven by cold-hot temperature alternation

Mingzi Chen

Zhejiang Normal University

Yanmin Jia (✉ ymjia@zjnu.edu.cn)

Zhejiang Normal University

Huamei Li

Zhejiang Normal University

Zheng Wu

Zhejiang Normal University

Tianyin Huang

Suzhou University of Science and Technology

Hongfang Zhang

Suzhou University of Science and Technology

Research Article

Keywords: Pyroelectric material, BiFeO₃, g-C₃N₄, Heterostructure, Pyrocatalysis

Posted Date: November 17th, 2020

DOI: <https://doi.org/10.21203/rs.3.rs-59738/v2>

License: © ⓘ This work is licensed under a Creative Commons Attribution 4.0 International License.

[Read Full License](#)

The enhanced pyrocatalysis of the pyroelectric BiFeO₃/g-C₃N₄ heterostructure for dye decomposition driven by cold-hot temperature alternation

Mingzi CHEN^{a,b}, Yanmin JIA^{a,b,*}, Huamei Li^a, Zheng WU^{c,*}, Tianyin HUANG^d,
Hongfang ZHANG^{d,*}

^a College of Physics and Electronic Information Engineering, Zhejiang Normal University, Jinhua
321004, China

^b School of Science, Xi'an University of Posts and Telecommunications, Xi'an 710121, China

^c College of Environmental and Chemical Engineering, Xi'an Polytechnic University, Xi'an 710048,
China

^d Jiangsu Key Laboratory of Micro and Nano Heat Fluid Flow Technology and Energy Application,
School of Physical Science and Technology and School of Environmental Science and Engineering,
Suzhou University of Science and Technology, Suzhou, 215009, China

*Corresponding Author: ymjia@zjnu.edu.cn (Y. Jia); wuzheng@xpu.edu.cn (Z. Wu);
constance_zhanghf@126.com (H. Zhang).

Abstract: The BiFeO₃/g-C₃N₄ heterostructure, which is fabricated via a simple mixing-calcining method, benefits the significant enhancement of the pyrocatalytic performance. With the growth of g-C₃N₄ content in the heterostructure pyrocatalysts from 0 to 25 %, the decomposition ratio of Rhodamine B (RhB) dye after 18 cold-hot temperature fluctuation (25 °C - 65 °C) cycles increases at first and then decreases, reaching a maximum value of ~ 94.2 % at 10 % while that of the pure BiFeO₃ is ~ 67.7 %. The enhanced dye decomposition may be due to the generation of the internal electric field which strengthens the separation of the positive and negative carriers and further

accelerates their migrations. The intermediate products in the pyrocatalytic reaction also have been detected and confirmed, which proves the key role of the pyroelectric effect in realizing the dye decomposition using BiFeO₃/g-C₃N₄ heterostructure catalyst. The pyroelectric BiFeO₃/g-C₃N₄ heterostructure shows the potential application in pyrocatalytically degrading dye wastewater.

Keywords: Pyroelectric material; BiFeO₃; g-C₃N₄; Heterostructure; Pyrocatalysis.

1 Introduction

The limited clean water has been seriously polluted by a large number of the chemical dyes discharged from the textile and printing industries, which results in a heavy environmental crisis [1, 2]. Photocatalysis, as an advanced oxidation technology, in which the clean solar energy can drive photocatalyst to generate free radicals in the end to degrade pollutants, has been widely reported for wastewater treatment [3], which has been widely reported for wastewater treatment [4, 5]. However, the disadvantages of no response in darkness and the high requirements on the light's transmission condition limit the practical application of photocatalysis in the dye decomposition [6]. Temperature fluctuation, as a great source of the thermal energy, can change the internal polarization intensity of the pyroelectric materials so that a charge imbalance forms between the internal polarization charges and the external compensation charges, leading to the separation and migration of these pyroelectrically-induced positive and negative charges to the surface of catalyst. Then, the pyroelectrically-induced charges react with hydroxyl ions and the dissolved oxygens to form the active free radicals with the strong oxidizing properties to decompose dye molecules [7, 8].

Recently, pyrocatalysis becomes increasingly popular in the dye decomposition [8-10]. Wu *et al.* have reported that the BiFeO₃ nanoparticles can decompose ~ 99 % Rhodamine B (RhB) dye after 85

cold-hot cycles [8]. Xu *et al.* have realized the decomposition ratio of $\sim 99\%$ for RhB dye after 50 cold-hot cycles with $\text{Ba}_{0.7}\text{Sr}_{0.3}\text{TiO}_3@1.5\%\text{Ag}$ nanoparticles [9]. You *et al.* have reported a decomposition ratio of RhB dye up to $\sim 86.5\%$ after 80 min with NaNbO_3 nanofibers in response to vibration together with cold-hot cycles [10]. How to further enhance the pyrocatalytic performance of the pyroelectric materials is crucial to their practical application in dye decomposition.

The method of fabricating heterostructure with the narrow-gap semiconductors to enhance catalytic performance has been widely applied in photocatalysis [11-13]. Benefitting from the generation of internal electric field on the interface, the heterostructure can strengthen the separation of the positive and negative carriers and further accelerate their migrations [14-16]. Therefore, this method may be available to enhance the pyrocatalytic performance of the pyroelectric materials in theory, which is rarely reported.

Graphitic carbon nitride ($\text{g-C}_3\text{N}_4$), as an organic semiconductor material, can be regarded as an ideal narrow-gap semiconductor option in the heterostructure due to its narrow band gap ($E_g = 2.7$ eV), metal-free property, great thermal and chemical stability [17-20]. Fabricating heterostructure with $\text{g-C}_3\text{N}_4$ has been widely used for improving the catalytic performance in the photocatalytic technology while its reports in pyrocatalysis field are rare up to now [21-23].

In our previous works, it has been reported that the pyroelectric materials of BaTiO_3 nanofibers [24], $\text{Pb}(\text{Zr}_{0.52}\text{Ti}_{0.48})\text{O}_3$ ceramics [7], ZnO nanorods [25] and NaNbO_3 nanorods [26] can respectively decompose $\sim 99\%$, $\sim 98\%$, $\sim 98\%$ and $\sim 96\%$ of RhB dye under the cold-hot cycles. Besides dye decomposition, other application of pyrocatalysis such as H_2 evolution [27, 28] has been realized. Some methods to enhance the pyrocatalytic performance have been developed such as the noble metal loading [29], fabricating heterostructures [30] and the optimizing poling field treatment [31].

In this work, a significantly-enhanced photocatalytic performance is found in the pyroelectric BiFeO₃/g-C₃N₄ heterostructure catalysts, which are fabricated via a simple mixing-calcining method. With the growth of g-C₃N₄ content in the heterostructure photocatalysts from 0 to 25 %, the decomposition ratio of Rhodamine B (RhB) dye after 18 cold-hot 25- 65 °C temperature fluctuation cycles increases at first and then decreases, reaching a maximum value of ~ 94.2 % at 10 % while that of the pure BiFeO₃ is ~ 67.7 %.

2 Materials and method

2.1 Synthesis of BiFeO₃

All the raw materials were analytical reagents in this experiment. BiFeO₃ was synthesized through a hydrothermal method [32, 33]. 2.425 g of Bi(NO₃)₃·5H₂O was dissolved in 50 mL of ethylene glycol. After the continuous magnetic stirring for 0.5 h, 1.352 g of FeCl₃·6H₂O and 200 mL of deionized water were added into the mixed solution. Then, NH₃·H₂O was added dropwise until the pH value of the solution up to ~ 11. The product in the solution was centrifuged out and then washed with the deionized water until its pH value fell to ~ 7. Thereafter, the washed product was put into 40 mL of 5 M NaOH with the continuous magnetic stirring for 0.5 h. Finally, the mixture solution was put into a teflon-lined stainless steel autoclave and heated at 140 °C for 72 h to obtain BiFeO₃.

2.2 Fabrication of BiFeO₃/g-C₃N₄ heterostructure

To obtain g-C₃N₄, 10 g of melamine was calcined in a muffle at 550 °C for 4 h with a heating rate of 5 °C/min [17]. To fabricate the BiFeO₃/g-C₃N₄ heterostructure, a certain amount of the prepared g-C₃N₄ and BiFeO₃ were dispersed in the absolute ethanol with the magnetic stirring for 0.5 h. Then, the mixture product was gained via centrifuge and dried at 70 °C for 12 h. Finally, it was placed into

a muffle and calcining at 400 °C for 4 h. Based on this method, BiFeO₃/g-C₃N₄ heterostructures with different g-C₃N₄ weight fractions of 0 %, 5 %, 10 %, 15 %, 20 %, 25 % were obtained.

2.3 Characterization

An X-ray diffractometer (XRD, Rigaku MiniFlex/600 powder, Japan) was employed to characterize the crystal structures of samples. The infrared spectra of samples were recorded on a fourier transform infrared spectrometer (FTIR, Nicolet iS5, USA). The microstructure characterizations of samples were conducted through a scanning electron microscopy (SEM, Phenom ProX, the Netherlands) and a transmission electron microscope (TEM, Tecnai G2 F20 S-Twin, USA) with a high resolution transmission electron microscope (HRTEM). The pyrocatalytic decomposition performances of BiFeO₃/g-C₃N₄ heterostructure catalysts for RhB dye were measured via a UV-vis spectrophotometer (Ocean Optics QE65Pro, USA).

2.4 Pyrocatalytic dye decomposition

In this experiment, all the pyrocatalytic reactions were carried out in darkness to avoid the influence of photocatalysis on the RhB dye decomposition. 50 mg of BiFeO₃/g-C₃N₄ heterostructure catalyst and 50 mL of RhB aqueous solution (5 mg/L) were added into a brown bottle with the magnetic stirring for 1 h to achieve an absorption equilibrium. A single cold-hot temperature fluctuation cycle was carried out between 25 °C and 65 °C with a 10 min heating and 10 min cooling. The brown bottle with the RhB dye solution and the BiFeO₃/g-C₃N₄ heterostructure catalyst was placed in the middle of a water bath container (RCT-B-S25, IKA, Germany) to realize the cold-hot temperature fluctuation between 25 °C and 65 °C [6, 34]. The temperature was monitored via a thermometer placed in the middle of the mechanically-stirred dye solution [9]. After every 3 cycles, 3 mL of the mixture solution was taken out and centrifugalized for the UV-vis spectra measurements.

3 Results and discussion

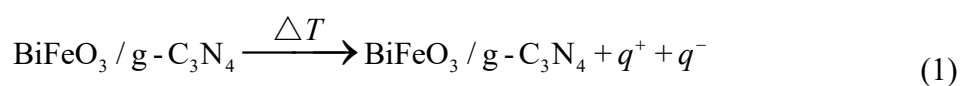
Fig. 1 (a) shows the XRD patterns of BiFeO₃/g-C₃N₄ heterostructures as well as the pure BiFeO₃. The diffraction peaks of the pure BiFeO₃ accord well with the rhombohedral phase based on the JCPDS Card No. 86-1518 [32]. Because of the low g-C₃N₄ content, there is no obvious difference of the XRD patterns between BiFeO₃/g-C₃N₄ heterostructures and the pure BiFeO₃ can be seen in Fig. 1 (a) [21, 33, 35].

The FTIR spectra of the pure BiFeO₃, BiFeO₃/10%g-C₃N₄ heterostructure and g-C₃N₄ are employed to confirm the existence of g-C₃N₄ in BiFeO₃/g-C₃N₄ heterostructure, as shown in Fig. 1 (b). The pure BiFeO₃ displays two obvious infrared signal peaks at ~ 484 and ~ 592 cm⁻¹, attributing to the O-Fe-O bending vibrations and the Fe-O stretching of FeO₆ groups in BiFeO₃ [35, 36]. With regard to g-C₃N₄, the peak at ~ 802 cm⁻¹ is ascribed to the out-of-plane bending modes of C-N heterocycles [37, 38]. In the range of 1200 - 1600 cm⁻¹, several strong infrared signal peaks are seen clearly from the curve of g-C₃N₄, corresponding to the C=N and the aromatic C-N stretching vibration modes [39, 40]. The characteristic infrared signal peaks of g-C₃N₄ and the pure BiFeO₃ also exhibit in the infrared spectrum of BiFeO₃/10%g-C₃N₄ heterostructure, revealing the great combination between g-C₃N₄ and the pure BiFeO₃.

The photocatalytic mechanism with BiFeO₃/g-C₃N₄ heterostructure catalyst is proposed in Fig. 2. BiFeO₃ is a kind of crystal that possesses a spontaneous polarization property. While it keeps a thermal equilibrium with the external medium, its internal polarization charges are shielded by the external compensation charges so that BiFeO₃ shows the electroneutrality. Once the thermal equilibrium is broken, temperature fluctuation changes the electric dipole moment of BiFeO₃,

which leads to the variation of the intensity of internal polarization. Therefore, a charge imbalance forms between the internal polarization charges and the external compensation charges [8]. It has been reported that the BiFeO₃ is a kind of *n*-type semiconductor ($E_g = \sim 2.2$ eV) while g-C₃N₄ behaves as an *p*-type semiconductor ($E_g = \sim 2.7$ eV) [41-43]. On the interface of the heterostructure, both the conduction band (CB) potential difference and the valence band (VB) potential difference between BiFeO₃ and g-C₃N₄ drive the electrons to diffuse from the CB of *n*-type BiFeO₃ to that of *p*-type g-C₃N₄, while on the contrary, holes diffuse from the VB of *p*-type g-C₃N₄ to that of *n*-type BiFeO₃ [44-46]. The diffusion of these carriers generates the negative charge center on the interface of g-C₃N₄ and the positive charge center on the interface of BiFeO₃, leading to the formation of the internal electric field, which further accelerates the separation of pyroelectrically-induced positive and negative charges, and the migration of pyroelectrically-induced positive charges from BiFeO₃ to g-C₃N₄.

Then, these pyroelectrically-induced charges react with hydroxyl ions and the dissolved oxygens on the surface of catalyst. The specific chemical equations in the photocatalytic reaction for dye decomposition with BiFeO₃/g-C₃N₄ heterostructure catalysts can be expressed as Eqs. (1) - (4) [47]:



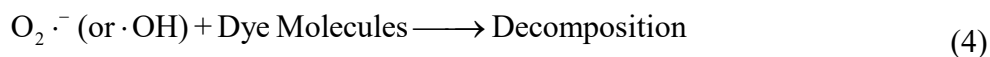
The dissolved oxygens (O₂) react with the pyroelectrically-induced negative charges (q^-) on the surface of BiFeO₃ to generate the superoxide radicals (O₂^{·-}) according to the Eq. (2):



Similarly, the pyroelectrically-induced positive charges (q^+) react with the hydroxyl ions (OH⁻) on the surface of g-C₃N₄ to form the hydroxyl radicals ([·]OH) based on Eq. (3):



Both the $\cdot\text{OH}$ and $\text{O}_2\cdot^-$ have the strong oxidizing properties to decompose dye molecules on the basis of Eq. (4):



The pure BiFeO_3 of a square nanosheet structure with an average width of ~ 600 nm and the $\text{g-C}_3\text{N}_4$ of a layer structure are clearly seen in the SEM images of Fig. 3(a) and Fig. 3(b). The small size of BiFeO_3 is beneficial for enlarging the surface area for reaction and shortening the migration distance for the pyroelectrically-induced charges to reach the surface of catalyst [7, 48]. BiFeO_3 presents the similar morphology in Fig. 3(a) and Fig. 3(b), indicating that the formation of heterostructure do not significantly affect the square nanosheet structure of BiFeO_3 [49]. Fig. 3(c) exhibits the TEM image of the $\text{BiFeO}_3/\text{g-C}_3\text{N}_4$ heterostructure. The square nanosheet structure of BiFeO_3 shown in Fig. 3(c) is in keeping with the observed morphology in the SEM images in Fig. 3(a) and Fig. 3(b). As displayed in Fig. 3(d), the HRTEM is employed to further confirm the microstructure of BiFeO_3 and the combination between $\text{g-C}_3\text{N}_4$ and BiFeO_3 . The lattice fringe in BiFeO_3 is ~ 0.433 nm, which is in line with the (0 1 2) crystal plane of BiFeO_3 . The interface between $\text{g-C}_3\text{N}_4$ and BiFeO_3 is presented clearly in the HRTEM image while its enlarged image inset shows the extremely close attachment of two materials as well.

The photocatalytic performances of $\text{BiFeO}_3/\text{g-C}_3\text{N}_4$ heterostructure catalysts are evaluated via the decomposition of RhB dye under cold-hot temperature fluctuation cycles. Fig. 4 shows the UV-vis absorption spectra of RhB dye solution with $\text{BiFeO}_3/\text{g-C}_3\text{N}_4$ heterostructure catalysts at different temperature fluctuation (between 25 °C and 65 °C) cycles shown in the inset of Fig. 4 (a). The absorption peak locating at ~ 554 nm decreases obviously with the increase of the cycle, indicating a

rapid decomposition of RhB dye. After undergoing 18 cycles, the BiFeO₃/10%g-C₃N₄ heterostructure catalyst displays an extremely weak signal of the absorption peak at ~ 554 nm, suggesting a nearly complete decomposition of RhB dye.

As the BiFeO₃/g-C₃N₄ heterostructure catalysts have demonstrated a obvious decomposition of RhB dye, it's necessary to further estimate their photocatalytic decomposition performances. The corresponding degradation ratios (*D*) of RhB dye over BiFeO₃/g-C₃N₄ heterostructure catalysts are calculated via Eq. (5):

$$D = (1 - C / C_0) \times 100 \% \quad (5)$$

Where the *C*₀ and *C* are the initial concentration and the current concentration of RhB dye solution, respectively [50]. Fig. 5 (a) exhibits the decomposition ratios of RhB dye at different cycles with BiFeO₃/g-C₃N₄ heterostructure catalysts. After 18 cycles, the BiFeO₃/g-C₃N₄ heterostructure catalysts with different g-C₃N₄ contents of 0 %, 5 %, 10 %, 15 %, 20 %, 25 % can respectively decompose ~ 67.7 %, ~ 76.7 %, ~ 94.2 %, ~ 91.7 %, ~ 87.4 % of RhB dye. The dependence of decomposition ratio on the g-C₃N₄ content of BiFeO₃/g-C₃N₄ heterostructure catalysts is shown in the inset of Fig.5 (a). The decomposition ratio of RhB dye increases significantly with the heterostructure and as high as ~ 94.2 %, which is the highest decomposition ratio of RhB dye among the BiFeO₃/g-C₃N₄ heterostructure catalysts, can be achieved via BiFeO₃/10%g-C₃N₄ heterostructure catalyst. As the g-C₃N₄ content of BiFeO₃/g-C₃N₄ heterostructure catalysts increases from 0 to 10 %, the increasing g-C₃N₄ content leads to a growing number of the BiFeO₃/g-C₃N₄ heterostructure unit so that the decomposition ratio of RhB dye increases at the beginning. When the content of g-C₃N₄ exceeds 10 %, the g-C₃N₄ of a layer structure stacks with itself, which becomes a new recombination center on the one hand and reduces the number of the BiFeO₃/g-C₃N₄ heterostructure unit on the

other hand [51, 52]. Both the increasing recombination ratio and the decreasing heterostructure unit number eventually result in the decrease of the RhB dye decomposition ratio.

A kinetic analysis of the photocatalytic reaction for RhB dye decomposition with BiFeO₃/g-C₃N₄ heterostructure catalysts is exhibited in Fig. 5 (b). The results accord well with the pseudo first order kinetic function based on the Eq. (6) [53-55]:

$$\ln(C / C_0) = -K \cdot t \quad (6)$$

Where t and K are the cycle and the kinetic rate constant in the photocatalytic reaction, respectively. The dependence of K on the g-C₃N₄ content of BiFeO₃/g-C₃N₄ heterostructure catalysts can be found in the inset of Fig. 5 (b). As the g-C₃N₄ content of BiFeO₃/g-C₃N₄ heterostructure catalysts grows from 0 to 25 %, the value of K increases at first and then decreases, giving a maximum value of $\sim 0.1513 \text{ cycle}^{-1}$ at 10 %, which is about 3 times as high as the K value of the pure BiFeO₃ ($\sim 0.0686 \text{ cycle}^{-1}$). The larger K value means the better photocatalytic performance of the BiFeO₃/g-C₃N₄ heterostructure catalyst. All BiFeO₃/g-C₃N₄ heterostructure catalysts behave the better photocatalytic performance than the pure BiFeO₃, while the optimal performance appears at the g-C₃N₄ content of 10 % in heterostructure catalyst.

The decomposition ratios of RhB dye with different catalysts and under various experimental conditions are shown in Fig.6. In the absence of BiFeO₃/10%g-C₃N₄ heterostructure catalyst, RhB dye solution shows almost no decomposition, which presents the excellent stability of RhB dye and excludes the influence of temperature fluctuation on RhB dye decomposition. Without temperature fluctuation, no obvious decomposition of RhB dye can be observed with BiFeO₃/10%g-C₃N₄ heterostructure catalyst, revealing the essential role of the temperature fluctuation in photocatalytic reaction. When BiFeO₃/10%g-C₃N₄ heterostructure catalyst is replaced with the corresponding

masses of BiFeO₃ and g-C₃N₄, the decomposition ratio of RhB dye becomes almost the same as that of using the pure BiFeO₃, which further proves the formation of the heterostructure and its indispensable role played in the significantly-enhanced photocatalytic performance.

In order to detect the intermediate products that play an important role in the photocatalytic decomposition of RhB dye, the photocatalytic experiments are carried out through adding different kinds of scavengers respectively. As shown in Fig. 7 (a), the decomposition ratios of RhB using BiFeO₃/10%g-C₃N₄ heterostructure catalyst with different kinds of scavengers decrease in different degrees. The lower decomposition ratio of RhB dye means the stronger inhibition effect of scavenger to the catalyst's photocatalytic performance. Ethylene diamine tetraacetic acid (EDTA), benzoquinone (BQ) and tert-butyl alcohol (TBA) are the scavenger of hole, O₂^{·-} and ·OH, respectively [56]. Therefore, holes, ·OH and O₂^{·-} are the main intermediate products in the photocatalytic reaction, while the lowest decomposition ratio of RhB dye using BiFeO₃/10%g-C₃N₄ heterostructure catalyst with BQ suggests that the O₂^{·-} is the most crucial active substance among them.

The recycling utilization results of the BiFeO₃/g-C₃N₄ heterostructure catalyst for RhB dye decomposition can be seen from Fig. 7 (b). After 18 cold-hot cycles, the BiFeO₃/10%g-C₃N₄ heterostructure catalyst was centrifuged out from the dye solution and washed with the deionized water. Then, it was dried at 70 °C for 12 h in an air oven and added into 50 mL of 5 mg/L RhB dye solution for the next 18 cycles. There is a slight decrease of the decomposition ratio after recycling the catalyst for 3 times, indicating the remarkable stability of its photocatalytic decomposition performance for RhB dye [57]. Furthermore, as a magnetic material, BiFeO₃ also has been reported with the excellent recyclable ability [58], which makes the recycling process of the catalyst convenient. Both the remarkable stability and the excellent recyclability of BiFeO₃/g-C₃N₄

heterostructure catalyst are helpful to its practical application in dye decomposition.

4 Conclusions

The significantly-enhanced photocatalytic performance is realized via the BiFeO₃/g-C₃N₄ heterostructure, which is fabricated through a simple mixing-calcining method. The decomposition ratio of RhB dye using the BiFeO₃/10%g-C₃N₄ heterostructure catalyst is about 30 % higher than that using the pure BiFeO₃. The main intermediate products in the photocatalytic reaction for RhB dye decomposition are detected and confirmed, among which the O₂^{·-} shows the most crucial influence. No obvious loss of the photocatalytic performance can be observed after recycling the catalyst for 3 times. The significantly-enhanced photocatalytic performance makes BiFeO₃/g-C₃N₄ heterostructure catalysts to have the potential in dealing with wastewater through utilizing the thermal energy of temperature fluctuation.

Acknowledgements

This work was supported by the National Natural Science Foundation of China (No. 51872264, 51778391), Shaanxi Provincial National Science Foundation of China (2020JM-579), Key Research and Development Program of Shaanxi Province, China (Grant No. 2020GXLH-Z-032), and the Basic Public Welfare Research Program of Zhejiang Province, China (LGG18E020005).

[1] H. Lin, Z. Wu, Y. Jia, *et al.* Piezoelectrically induced mechano-catalytic effect for degradation of dye wastewater through vibrating Pb(Zr_{0.52}Ti_{0.48})O₃ fibers. *Appl Phys Lett* 2014, **104**: 162907.

[2] A. Sadeghzadeh-Attar. Photocatalytic degradation evaluation of N-Fe codoped aligned TiO₂

- nanorods based on the effect of annealing temperature. *J Adv Ceram* 2020, **9**: 107-122.
- [3] K. Nakata, A. Fujishima, TiO₂ photocatalysis: design and applications. *J Photoch. Photobio C* 2012, **13**(3): 169-189.
- [4] Q. Li, T. Zhao, M. Li, *et al.* One-step construction of pickering emulsion via commercial TiO₂ nanoparticles for photocatalytic dye degradation. *Appl Catal B: Environ* 2019, **249**: 1-8.
- [5] X. Xue, W. Zang, P. Deng, *et al.* Piezo-potential enhanced photocatalytic degradation of organic dye using ZnO nanowires. *Nano Energy* 2015, **13**: 414-422.
- [6] Z. Wu, W. Luo, H. Zhang, *et al.* Strong pyro-catalysis of shape-controllable bismuth oxychloride nanomaterial for wastewater remediation. *Appl Surf Sci* 2020, **513**: 145630.
- [7] J. Ma, L. Chen, Z. Wu, *et al.* Pyroelectric Pb(Zr_{0.52}Ti_{0.48})O₃ polarized ceramic with strong pyro-driven catalysis for dye wastewater decomposition. *Ceram Int* 2019, **45**: 11934-11938.
- [8] J. Wu, W. Mao, Z. Wu, *et al.* Strong pyro-catalysis of pyroelectric BiFeO₃ nanoparticles under a room-temperature cold-hot alternation. *Nanoscale* 2016, **8**: 7343-7350.
- [9] X. Xu, S. Chen, Z. Wu, *et al.* Strong pyro-electro-chemical coupling of Ba_{0.7}Sr_{0.3}TiO₃@Ag pyroelectric nanoparticles for room-temperature pyrocatalysis. *Nano Energy* 2018, **50**: 581-588.
- [10] H. You, X. Ma, Z. Wu, *et al.* Piezoelectrically/pyroelectrically-driven vibration/cold-hot energy harvesting for mechano-/pyro- bi-catalytic dye decomposition of NaNbO₃ nanofibers. *Nano Energy* 2018, **52**: 351-359.
- [11] N. Tian, H. Huang, S. Wang, *et al.* Facet-charge-induced coupling dependent interfacial photocharge separation: a case of BiOI/g-C₃N₄ p-n junction. *Appl Catal B: Environ* 2020, **267**: 118697.
- [12] Z. Zhang, W. Wang, L. Wang, *et al.* Enhancement of visible-light photocatalysis by coupling

with narrow-band-gap semiconductor: a case study on Bi₂S₃/Bi₂WO₆. *ACS Appl Mater Inter* 2012, **4**: 593-597.

[13] Y. Yue, P. Zhang, W. Wang, *et al.* Enhanced dark adsorption and visible-light-driven photocatalytic properties of narrower-band-gap Cu₂S decorated Cu₂O nanocomposites for efficient removal of organic pollutants. *J Hazard Mater* 2020, **384**: 121302.

[14] H. You, Z. Wu, Y. Jia, *et al.* High-efficiency and mechano-/photo-bi-catalysis of piezoelectric-ZnO@photoelectric-TiO₂ core-shell nanofibers for dye decomposition. *Chemosphere* 2017, **183**: 528-535.

[15] R. Marschall. Semiconductor composites: strategies for enhancing charge carrier separation to improve photocatalytic activity. *Adv Funct Mater* 2014, **24**: 2421-2440.

[16] J. Yu, Q. Nong, X. Jiang, *et al.* Novel Fe₂(MoO₄)₃/g-C₃N₄ heterojunction for efficient contaminant removal and hydrogen production under visible light irradiation. *Sol Energy* 2016, **139**: 355-364.

[17] Y. He, Y. Wang, L. Zhang, *et al.* High-efficiency conversion of CO₂ to fuel over ZnO/g-C₃N₄ photocatalyst. *Appl Catal B: Environ* 2015, **168-169**: 1-8.

[18] W. J. Ong, L.L. Tan, Y.H. Ng, *et al.* Graphitic carbon nitride (g-C₃N₄)-based photocatalysts for artificial photosynthesis and environmental remediation: are we a step closer to achieving sustainability? *Chem Rev* 2016, **116**: 7159-7329.

[19] J. Zhu, P. Xiao, H. Li, *et al.* Graphitic carbon nitride: synthesis, properties, and applications in catalysis. *ACS Appl Mater Inter* 2014, **6**: 16449-16465.

[20] X. Dong, F. Cheng. Recent development in exfoliated two-dimensional g-C₃N₄ nanosheets for photocatalytic applications. *J Mater Chem A* 2015, **3**: 23642-23652.

- [21] T. Li, L. Zhao, Y. He, *et al.* Synthesis of g-C₃N₄/SmVO₄ composite photocatalyst with improved visible light photocatalytic activities in RhB degradation. *Appl Catal B: Environ* 2013, **129**: 255-263.
- [22] Z. Yang, J. Li, F. Cheng, *et al.* BiOBr/protonated graphitic C₃N₄ heterojunctions: Intimate interfaces by electrostatic interaction and enhanced photocatalytic activity. *J Alloy Compd* 2015, **634**: 215-222.
- [23] J. Fu, B. Chang, Y. Tian, *et al.* Novel C₃N₄-CdS composite photocatalysts with organic-inorganic heterojunctions: in situ synthesis, exceptional activity, high stability and photocatalytic mechanism. *J Mater Chem A* 2013, **1**: 3083-3090.
- [24] Y. Xia, Y. Jia, W. Qian, *et al.* Pyroelectrically induced pyro-electro-chemical catalytic activity of BaTiO₃ nanofibers under room-temperature cold-hot cycle excitations. *Metals* 2017, **7**: 122.
- [25] W. Qian, Z. Wu, Y. Jia, *et al.* Thermo-electrochemical coupling for room temperature thermocatalysis in pyroelectric ZnO nanorods. *Electrochem Commun* 2017, **81**: 124-127.
- [26] H. You, Z. Wu, L. Wang, *et al.* Highly efficient pyrocatalysis of pyroelectric NaNbO₃ shape-controllable nanoparticles for room-temperature dye decomposition. *Chemosphere* 2018, **199**: 531-537.
- [27] H. You, Y. Jia, Z. Wu, *et al.* Room-temperature pyrocatalytic hydrogen generation of 2D few-layer black phosphorene under cold-hot alternation. *Nat Commun* 2018, **9**: 2889.
- [28] X. Xu, L. Xiao, Y. Jia, *et al.* Pyro-catalytic hydrogen evolution by Ba_{0.7}Sr_{0.3}TiO₃ nanoparticles: harvesting cold-hot alternation energy near room-temperature. *Environ Sci* 2018, **11**: 2198-2207.
- [29] J. Ma, W. Luo, Z. Wu, *et al.* High pyrocatalytic properties of pyroelectric BaTiO₃ nanofibers

loaded by noble metal under roomtemperature thermal cycling. *Ceram Int* 2018, **44**: 21835-21841.

[30] L. Wang, N.O. Haugen, Z. Wu, *et al.* Ferroelectric BaTiO₃@ZnO heterostructure nanofibers with enhanced pyroelectrically-driven-catalysis. *Ceram Int* 2019, **45**: 90-95.

[31] L. Chen, H. Li, Z. Wu, *et al.* Enhancement of pyroelectric catalysis of ferroelectric BaTiO₃ crystal: the action mechanism of electric poling. *Ceram Int* 2020, **46**: 16763-12769.

[32] H. You, Y. Jia, Z. Wu, *et al.* Strong piezo-electrochemical effect of multiferroic BiFeO₃ square micro-sheets for mechanocatalysis. *Electrochem Commun* 2017, **79**: 55-58.

[33] X. Wang, W. Mao, J. Zhang, *et al.* Facile fabrication of highly efficient g-C₃N₄/BiFeO₃ nanocomposites with enhanced visible light photocatalytic activities, *J Colloid Interf Sci* 2015, **448**: 17-23.

[34] X. Xu, L. Xiao, Y. Jia, *et al.* Pyro-catalytic hydrogen evolution by Ba_{0.7}Sr_{0.3}TiO₃ nanoparticles: harvesting cold-hot alternation energy near room-temperature. *Energy Environ Sci* 2018, **11**: 21982207.

[35] X. Hu, W. Wang, G. Xie, *et al.* Ternary assembly of g-C₃N₄/graphene oxide sheets/BiFeO₃ heterojunction with enhanced photoreduction of Cr (VI) under visible-light irradiation. *Chemosphere* 2019, **216**: 733-741.

[36] W. Luo, L. Zhu, N. Wang, *et al.* Efficient removal of organic pollutants with magnetic nanoscaled BiFeO₃ as a reusable heterogeneous fenton-like catalyst. *Environ Sci Technol* 2010, **44**: 1786-1791.

[37] Y. Zhang, Q. Zhang, Q. Shi, *et al.* Acid-treated g-C₃N₄ with improved photocatalytic performance in the reduction of aqueous Cr (VI) under visible-light. *Sep Purif Technol* 2015, **142**: 251-257.

- [38] H.W. Kang, S.N. Lim, D. Song, *et al.* Organic-inorganic composite of g-C₃N₄-SrTiO₃: Rh photocatalyst for improved H₂ evolution under visible light irradiation. *Int J Hydrogen Energ* 2012, **37**: 11602-11610.
- [39] Y. Su, Y. Zhao, Y. Zhao, *et al.* Novel ternary component Ag-SrTa₂O₆/g-C₃N₄ photocatalyst: synthesis, optical properties and visible light photocatalytic activity. *Appl Surf Sci* 2015, **358**: 213-222.
- [40] Z. Feng, L. Zeng, Y. Chen, *et al.* In situ preparation of Z-scheme MoO₃/g-C₃N₄ composite with high performance in photocatalytic CO₂ reduction and RhB degradation. *J Mater Res* 2017, **32**: 1-9.
- [41] H. You, Z. Wu, L. Zhang, *et al.* Harvesting the vibration energy of BiFeO₃ nanosheets for hydrogen evolution. *Angew Chem Int Edit* 2019, **58**: 11779-11784.
- [43] H. Gao, X. Zhao, H. Zhang, *et al.* Construction of 2D/0D/2D face-to-face contact g-C₃N₄@Au@Bi₄Ti₃O₁₂ heterojunction photocatalysts for degradation of Rhodamine B. *J Electron Mater* 2020, **49**: 5248-5259.
- [43] Y. Yan, H. Yang, Z. Yi, *et al.* Construction of Ag₂S@CaTiO₃ heterostructure photocatalysts for enhanced photocatalytic degradation of dyes. *Desalin Water Treat.* 2019, **170**: 349-360.
- [44] Y. Wang, H. Yang, X. Sun, *et al.* Preparation and photocatalytic application of ternary n-BaTiO₃/Ag/p-AgBr heterostructured photocatalysts for dye degradation. *Mater Res Bull* 2020, **124**: 110754.
- [45] L.J. Di, H. Yang, T. Xian, *et al.* Facile synthesis and enhanced visible-light photocatalytic activity of novel p-Ag₃PO₄/n-BiFeO₃ heterostructure composites for dye degradation. *Nanoscale Res Lett* 2018, **13**: 257.
- [46] Y. Yan, H. Yang, Z. Yi, *et al.* Design of ternary CaTiO₃/g-C₃N₄/AgBr Z-scheme

heterostructured photocatalysts and their application for dye photodegradation. *Solid State Sci* 2020, **100**: 106102.

[47] Y. Bai, J. Zhao, Z. Lv, *et al.* Enhanced piezocatalytic performance of ZnO nanosheet microspheres by enriching the surface oxygen vacancies. *J Mater Sci* 2020, **55**: 14112-14124.

[48] A.N. Morozovska, E.A. Eliseev, G.S. Svechnikov, *et al.* Pyroelectric response of ferroelectric nanowires: size effect and electric energy harvesting. *J Appl Phys* 2010, **108**: 042009.

[49] H. Liu, W. Cao, Y. Su, *et al.* Synthesis, characterization and photocatalytic performance of novel visible-light-induced Ag/BiOI. *Appl Catal B: Environ* 2012, **111-112**: 271-279.

[50] R. Pagano, C. Ingrosso, G. Giancane, *et al.* Wet synthesis of elongated hexagonal ZnO microstructures for applications as photo-piezoelectric catalysts. *Materials* 2020, **13**: 2938.

[51] X. Liu, L. Xiao, Y. Zhang, *et al.* Significantly enhanced piezo-photocatalytic capability in BaTiO₃ nanowires for degrading organic dye. *J Materiomics*, 2020, **6**: 256-262.

[52] H. Sun, Y. Liu, Y. Zhang, *et al.* Synthesis of Bi₂Fe₄O₉/reduced graphene oxide composite by one-step hydrothermal method and its high photocatalytic performance. *J Mater Sci: Mater El* 2014, **25** (10): 4212-4218.

[53] P. Liu, H. Sun, X. Liu, *et al.* Enhanced photocatalytic performance of Bi₂Fe₄O₉/graphene via modifying graphene composite. *J Am Ceram Soc* 2017, **100** (8): 3540-3549.

[54] Y. Zhang, H. Sun, W. Chen, Li-modified Ba_{0.99}Ca_{0.01}Zr_{0.02}Ti_{0.98}O₃ lead-free ceramics with highly improved piezoelectricity. *J Colloid Interf Sci* 2017, **694**: 745-751.

[55] Y. Zhang, H. Sun, W. Chen, A brief review of Ba(Ti_{0.8}Zr_{0.2})O₃-(Ba_{0.7}Ca_{0.3})TiO₃ based lead-free piezoelectric ceramics: past, present and future perspectives. *J Phys Chem Solids* 2018, **114**: 207-219.

[56] F. Meng, W. Ma, Y. Wang, *et al.* A tribo-positive Fe@MoS₂ piezocatalyst for the durable degradation of tetracycline: degradation mechanism and toxicity assessment. *Environ Sci: Nano* 2020, **7**: 1704-1718.

[57] Y. Chen, X. Deng, J. Wen, *et al.* Piezo-promoted the generation of reactive oxygen species and the photodegradation of organic pollutants. *Appl Catal B: Environ* 2019, **258**: 118024.

[58] Z.H. Jaffari, S.M. Lam, J.C. Sin, *et al.* Magnetically recoverable Pd-loaded BiFeO₃ microcomposite with enhanced visible light photocatalytic performance for pollutant, bacterial and fungal elimination. *Sep Purif Technol* 2020, **236**: 116195.

Figure Captions:

Fig. 1 (a) The XRD patterns of the pure BiFeO₃ and BiFeO₃/g-C₃N₄ heterostructures. (b) The FTIR spectra of the pure BiFeO₃, BiFeO₃/10%g-C₃N₄ heterostructure and g-C₃N₄.

Fig. 2 The schematic diagram of the photocatalytic reaction with BiFeO₃/g-C₃N₄ heterostructure catalyst.

Fig. 3 The SEM images of (a) the pure BiFeO₃ and (b) BiFeO₃/g-C₃N₄ heterostructure. (c) The TEM and (d) HRTEM images of BiFeO₃/g-C₃N₄ heterostructure.

Fig. 4 The UV-vis spectra of RhB dye solution after different numbers of cycles using BiFeO₃/g-C₃N₄ heterostructure catalysts. (a) The pure BiFeO₃. The inset is the ideal temperature fluctuation curve in the photocatalytic experiment. (b) BiFeO₃/5%g-C₃N₄. (c) BiFeO₃/10%g-C₃N₄. (d) BiFeO₃/15%g-C₃N₄. (e) BiFeO₃/20%g-C₃N₄. (f) BiFeO₃/25% g-C₃N₄.

Fig. 5 (a) The decomposition ratios of RhB dye after different numbers of cycles using BiFeO₃/g-C₃N₄ heterostructure catalysts. The inset shows the dependence of decomposition ratio on

the g-C₃N₄ content after 18 cycles. (b) The plot of the negative logarithm of C/C_0 versus cycles. The inset shows the dependence of the kinetic rate constant on the g-C₃N₄ content.

Fig. 6 The comparison of the decomposition ratios of RhB dye with different catalysts and under different reaction conditions.

Fig. 7 (a) The detection of intermediate products in the photocatalytic reaction using BiFeO₃/10%g-C₃N₄ heterostructure catalyst with different scavengers. (b) The recycling utilization of BiFeO₃/10%g-C₃N₄ heterostructure catalyst for RhB dye decomposition.

Figures

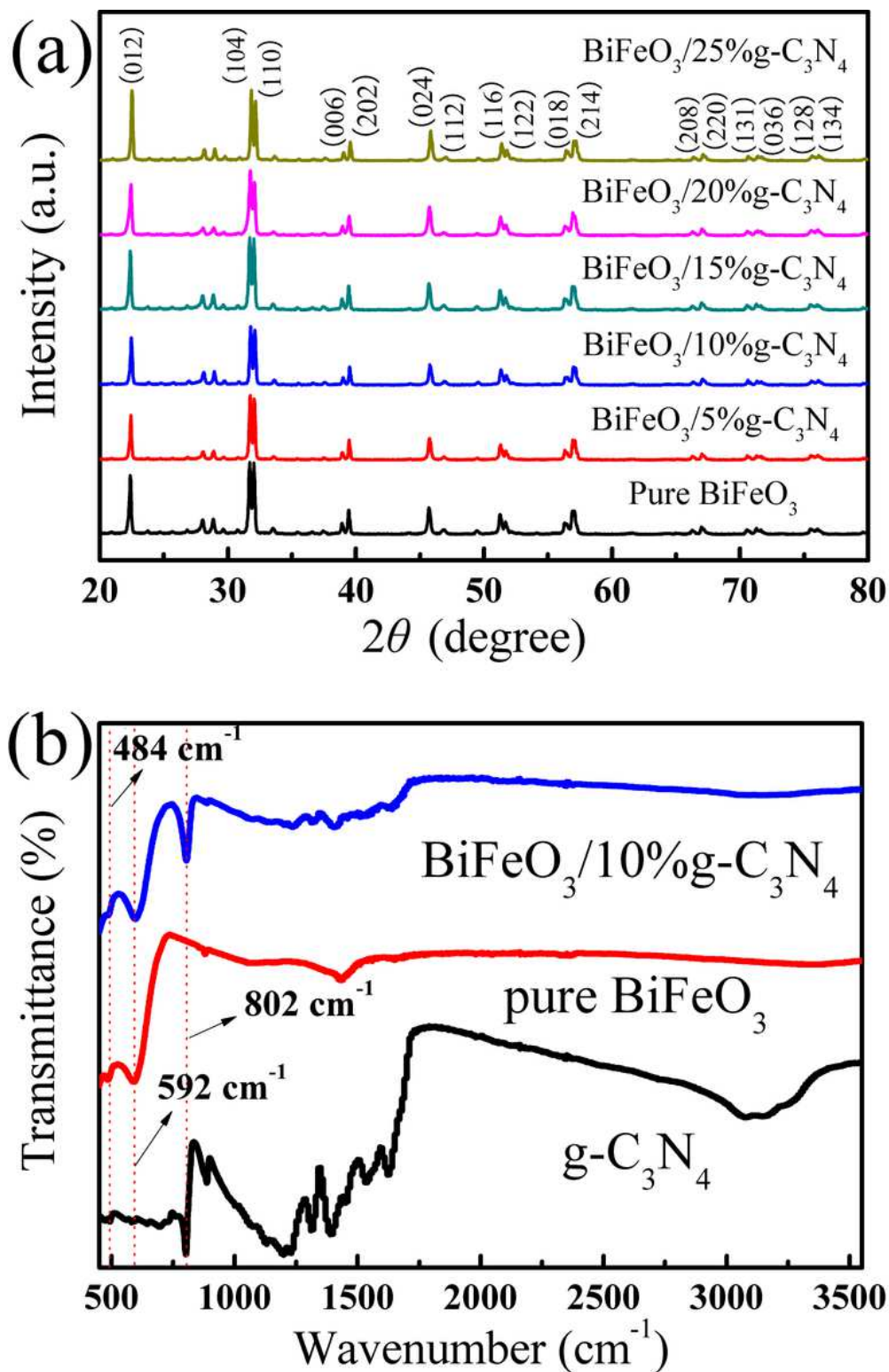


Figure 1

(a) The XRD patterns of the pure BiFeO₃ and BiFeO₃/g-C₃N₄ heterostructures. (b) The FTIR spectra of the pure BiFeO₃, BiFeO₃/10%g-C₃N₄ heterostructure and g-C₃N₄.

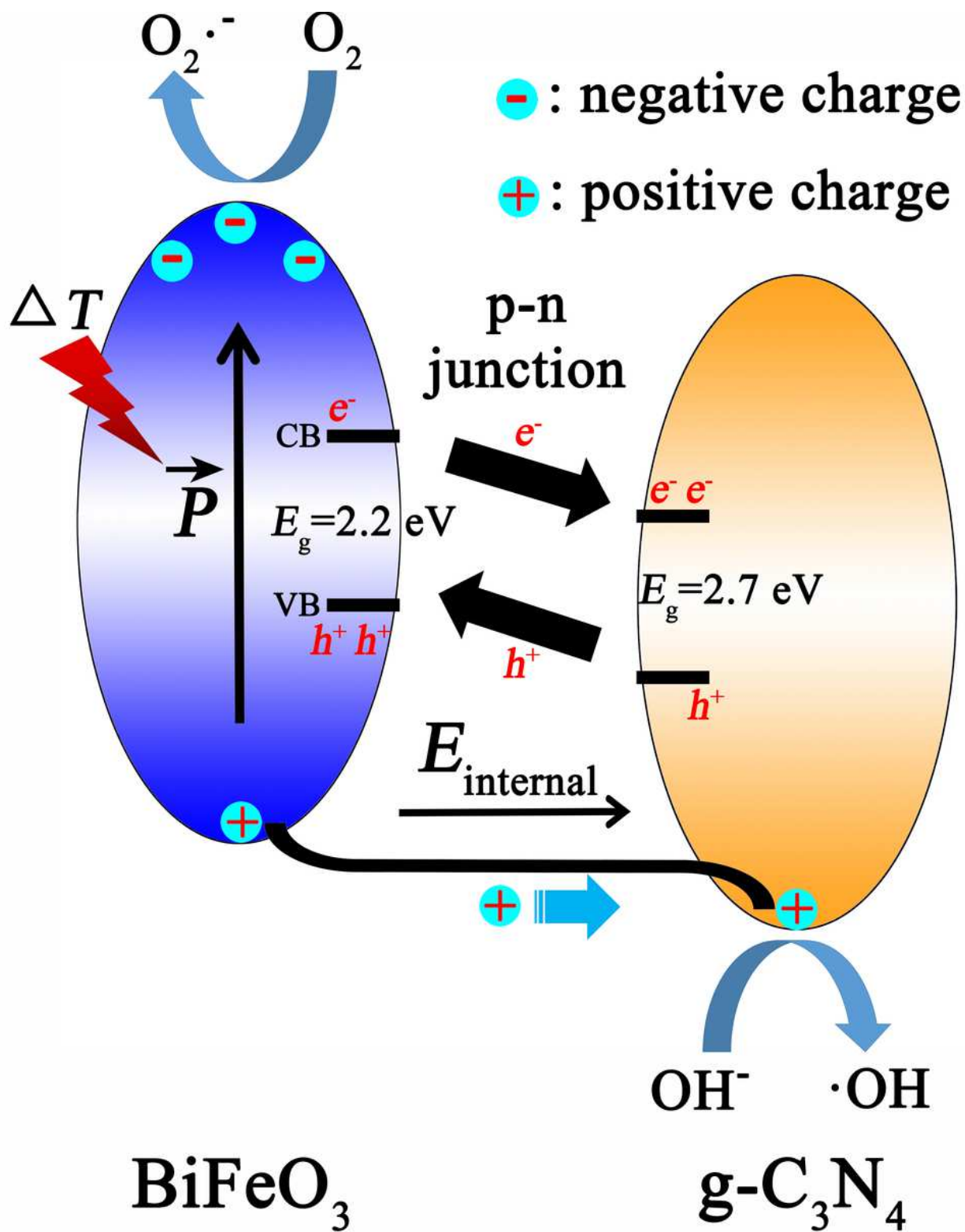


Figure 2

The schematic diagram of the photocatalytic reaction with BiFeO₃/g-C₃N₄ heterostructure catalyst.

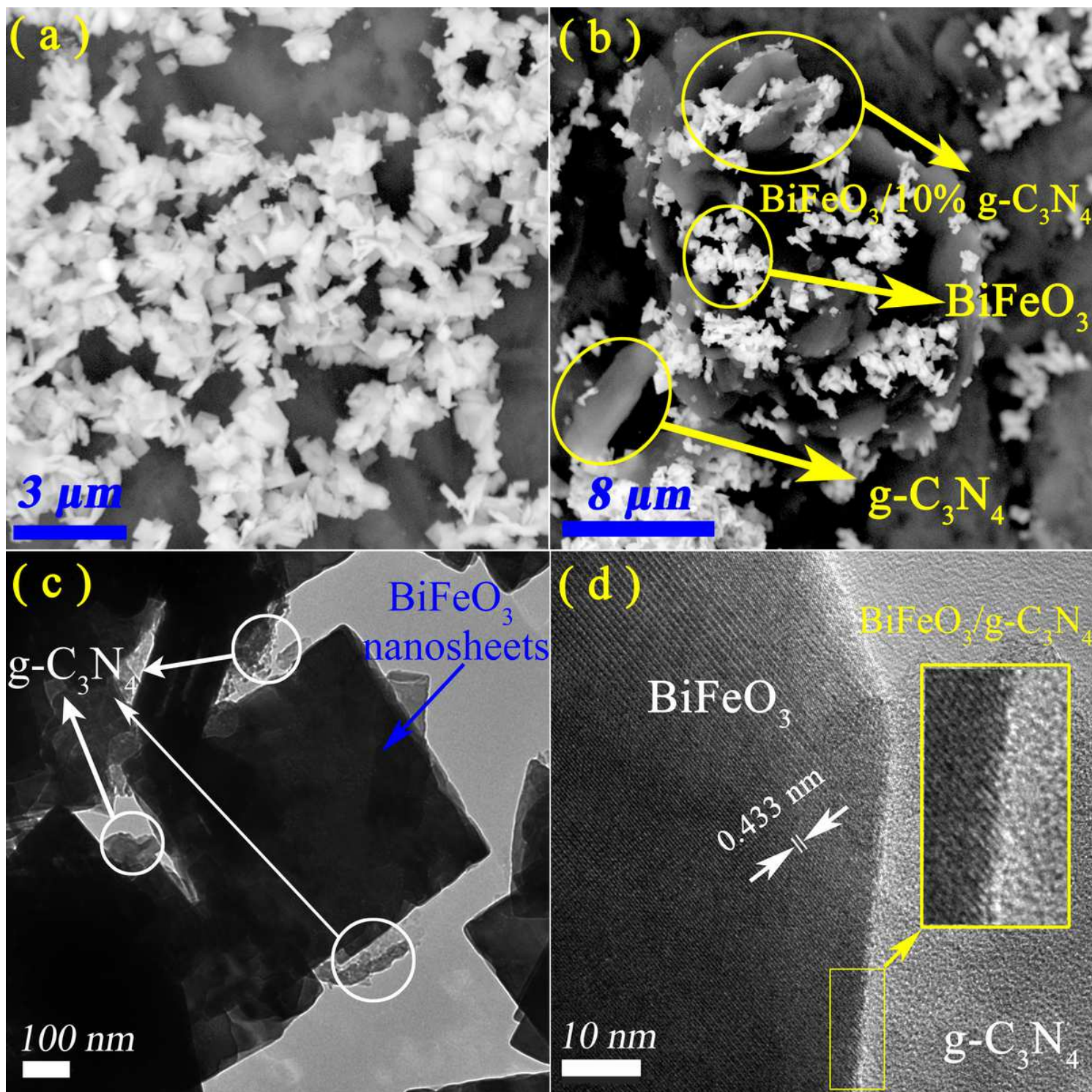


Figure 3

The SEM images of (a) the pure BiFeO₃ and (b) BiFeO₃/g-C₃N₄ heterostructure. (c) The TEM and (d) HRTEM images of BiFeO₃/g-C₃N₄ heterostructure.

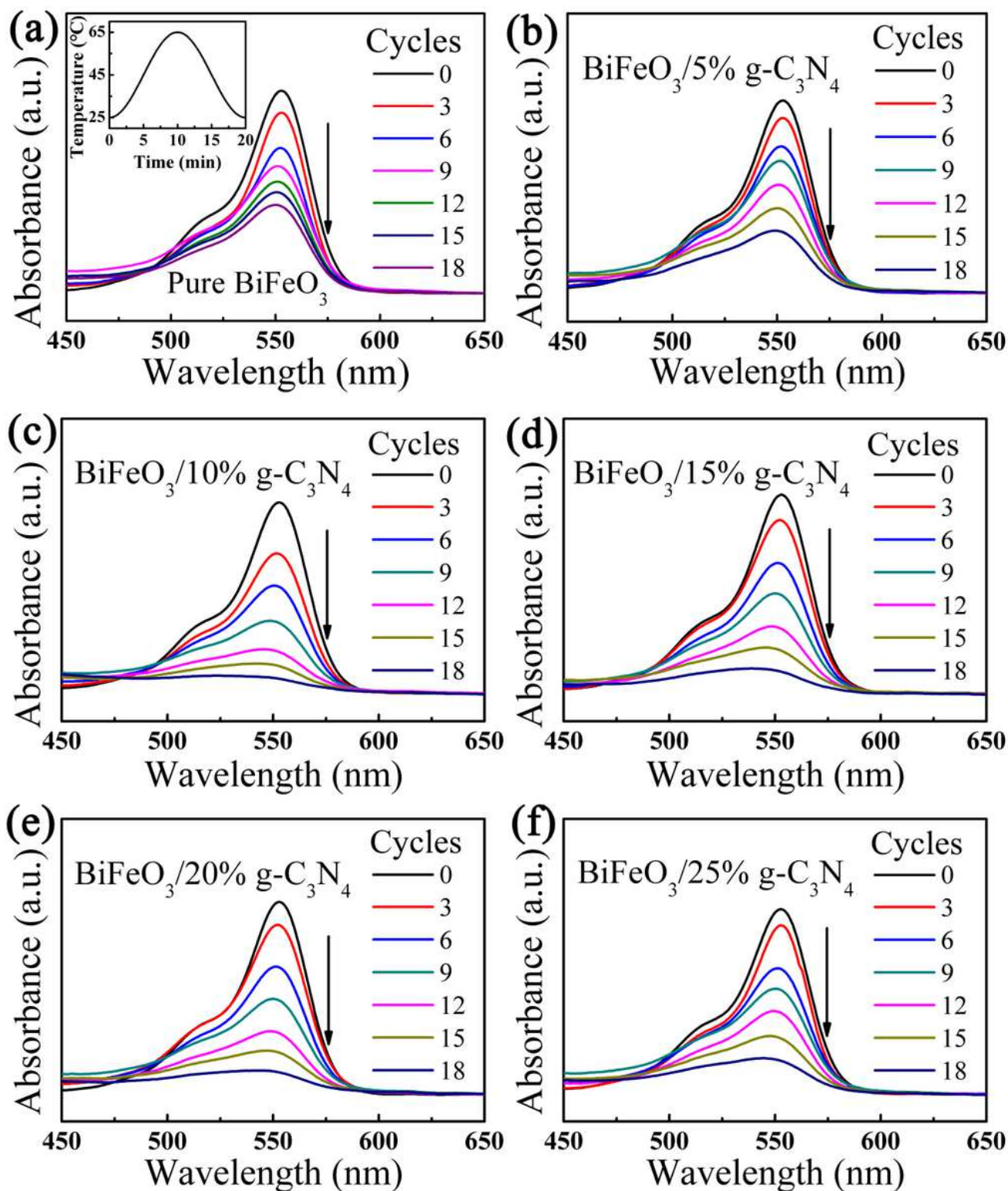


Figure 4

The UV-vis spectra of RhB dye solution after different numbers of cycles using BiFeO₃/g-C₃N₄ heterostructure catalysts. (a) The pure BiFeO₃. The inset is the ideal temperature fluctuation curve in the photocatalytic experiment. (b) BiFeO₃/5%g-C₃N₄. (c) BiFeO₃/10%g-C₃N₄. (d) BiFeO₃/15%g-C₃N₄. (e) BiFeO₃/20%g-C₃N₄. (f) BiFeO₃/25% g-C₃N₄.

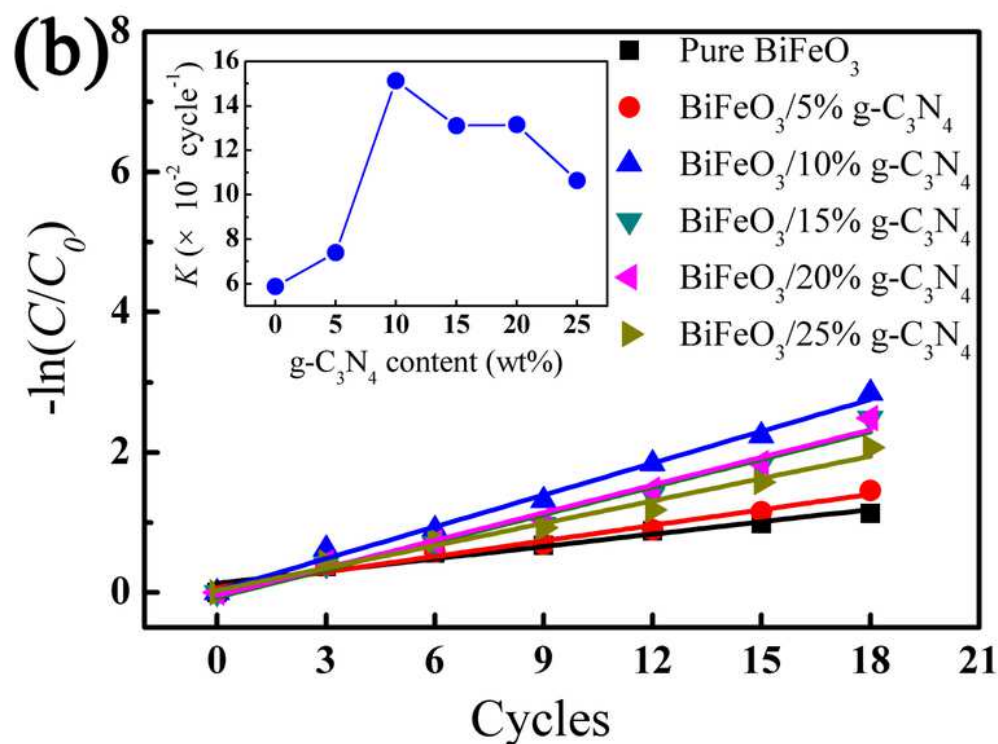
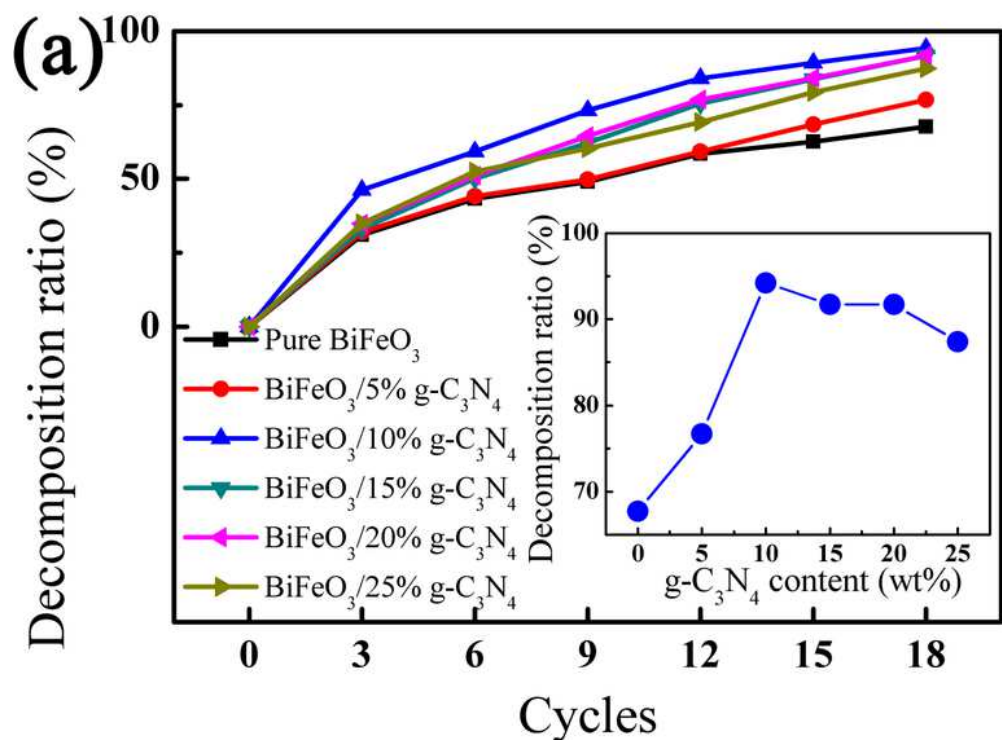


Figure 5

(a) The decomposition ratios of RhB dye after different numbers of cycles using BiFeO₃/g-C₃N₄ heterostructure catalysts. The inset shows the dependence of decomposition ratio on the g-C₃N₄ content after 18 cycles. (b) The plot of the negative logarithm of C/C₀ versus cycles. The inset shows the dependence of the kinetic rate constant on the g-C₃N₄ content.

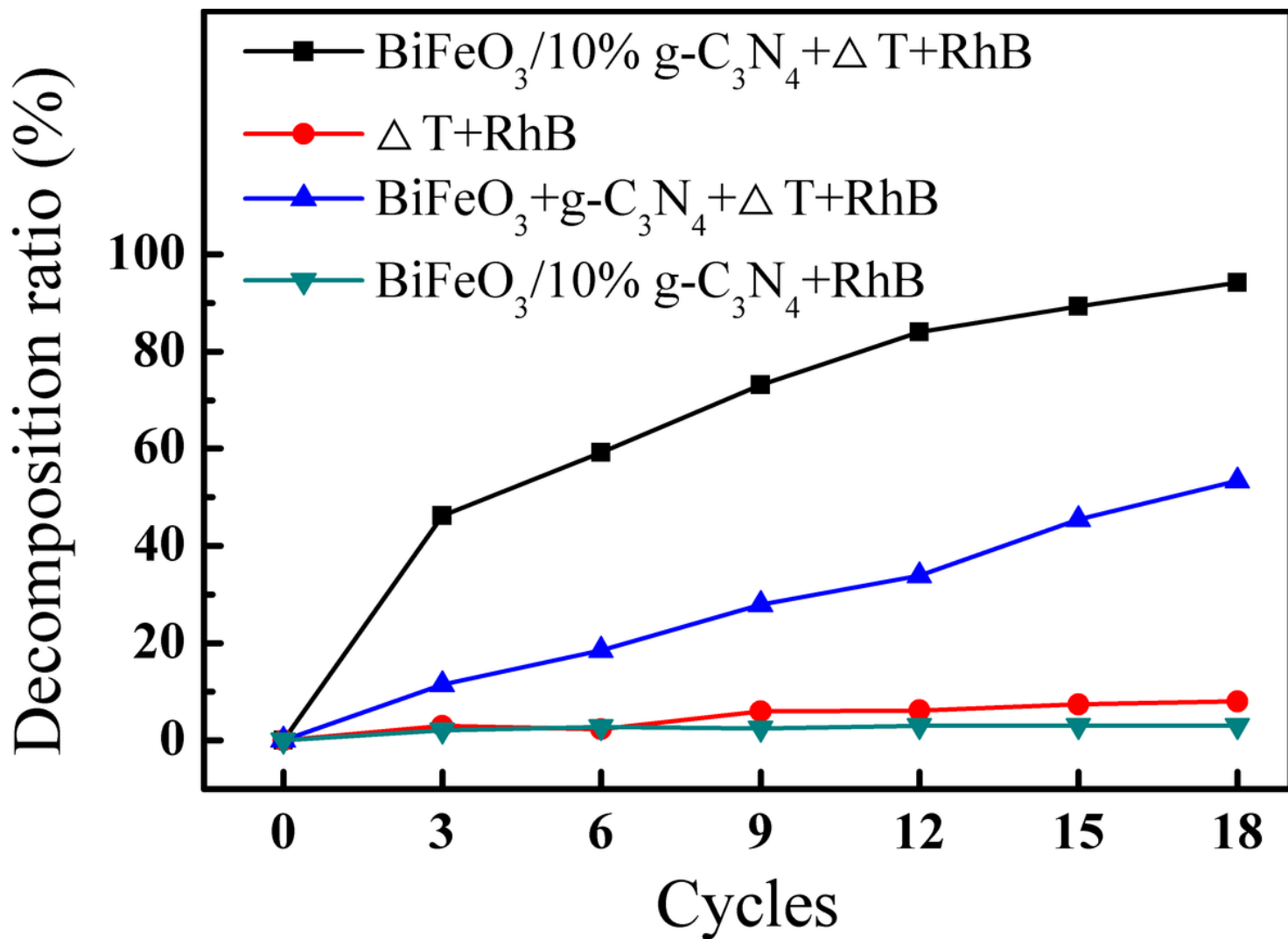


Figure 6

The comparison of the decomposition ratios of RhB dye with different catalysts and under different reaction conditions.

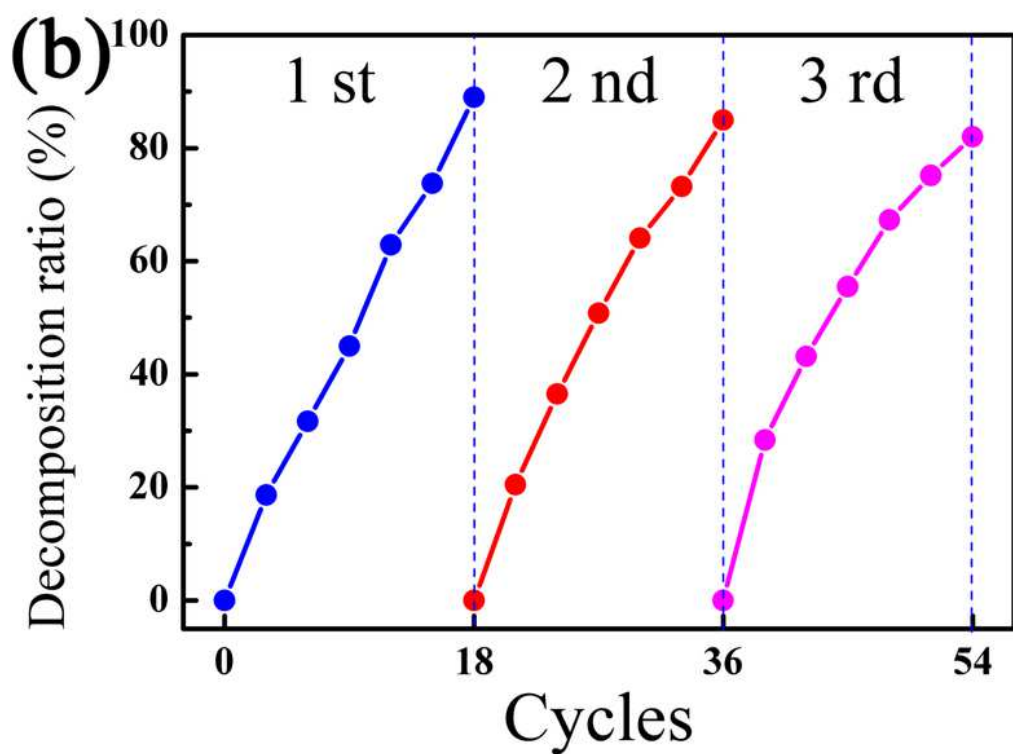
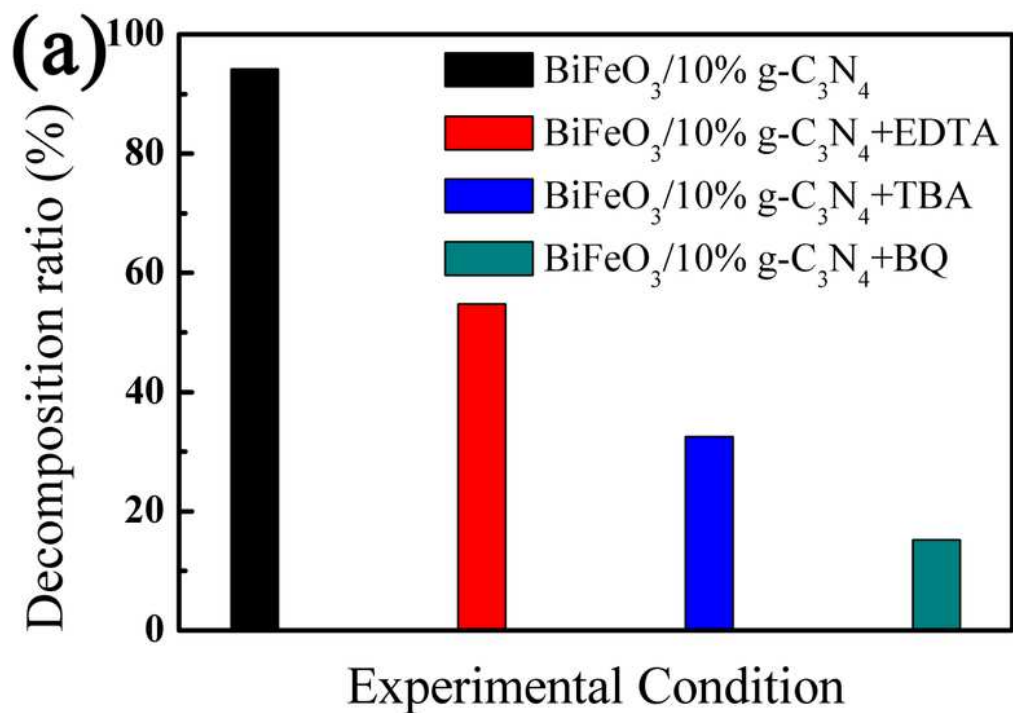


Figure 7

(a) The detection of intermediate products in the photocatalytic reaction using BiFeO₃/10%g-C₃N₄ heterostructure catalyst with different scavengers. (b) The recycling utilization of BiFeO₃/10%g-C₃N₄ heterostructure catalyst for RhB dye decomposition.

Supplementary Files

This is a list of supplementary files associated with this preprint. Click to download.

- [renameda0725.tif](#)